



Deposited via The University of Leeds.

White Rose Research Online URL for this paper:

<https://eprints.whiterose.ac.uk/id/eprint/146008/>

Version: Accepted Version

---

**Article:**

Al-Dirawi, KH and Bayly, AE (2019) A new model for the bouncing regime boundary in binary droplet collisions. *Physics of Fluids*, 31 (2). 027105. ISSN: 1070-6631

<https://doi.org/10.1063/1.5085762>

---

© 2019 Author(s). This article may be downloaded for personal use only. Any other use requires prior permission of the author and AIP Publishing. The following article appeared in Al-Dirawi, KH and Bayly, AE (2019) A new model for the bouncing regime boundary in binary droplet collisions. *Physics of Fluids*, 31 (2). 027105. ISSN 1070-6631 and may be found at <https://doi.org/10.1063/1.5085762>. Uploaded in accordance with the publisher's self-archiving policy.

**Reuse**

Items deposited in White Rose Research Online are protected by copyright, with all rights reserved unless indicated otherwise. They may be downloaded and/or printed for private study, or other acts as permitted by national copyright laws. The publisher or other rights holders may allow further reproduction and re-use of the full text version. This is indicated by the licence information on the White Rose Research Online record for the item.

**Takedown**

If you consider content in White Rose Research Online to be in breach of UK law, please notify us by emailing [eprints@whiterose.ac.uk](mailto:eprints@whiterose.ac.uk) including the URL of the record and the reason for the withdrawal request.

# **A new model for the bouncing regime boundary in binary droplet collisions**

Karrar H. Al-Dirawi and Andrew E. Bayly

*School of Chemical and Process Engineering, University of Leeds, Leeds, LS2 9JT, United Kingdom*

This work experimentally investigates binary collisions of identical droplets over a range of liquid viscosities, using 2%, 4%, and 8% of hydroxypropyl methylcellulose (HPMC) solutions in water. The collisions were captured by a high-speed camera, and regime maps of collision outcomes derived. The performance of existing models of the boundary of the bouncing regime was assessed and found to give poor predictions. This was attributed to assumptions and errors in the treatment of kinetic energy and the droplet shape factors used in these models. A new model was derived which addresses these issues: the definition of the kinetic energy that contributes to deformation was corrected; a new shape factor that accurately reflects the geometry of the droplet at maximum deformation was proposed and, importantly, an empirical approach was implemented to account for the effect of the impact parameter on this shape factor. Moreover, the model includes an estimate of the viscous dissipation, which is calculated directly from experimentally observed difference between the impact and the rebound kinetic energies, and measurements of the post-collision droplet oscillations. The proposed model shows a striking improvement versus the existing models, reducing the mean absolute error by an order of magnitude.

## **I. INTRODUCTION**

Droplet collisions are ubiquitous in natural phenomena and many industrial applications, such as atmospheric studies, combustion engines, and spray drying. Prediction of the collision outcome has a vital importance in these applications. For instance, spray drying is a process of converting slurries or solutions into dry powder. In this process the feed liquid is atomized in a drying chamber in which a turbulent hot air comes in contact with droplets. Consequently, droplet collisions occur and the outcomes of these collisions play an important role in the prediction of the tower performance and the product properties (Francia et al., 2017). A good understanding and accurate models of collision behavior is therefore important for the prediction of both process performance and product properties.

In the past few decades, a substantial amount of research has been conducted to construct regime maps for binary droplet systems, and to understand the fundamental criteria that lead to different collision outcomes (Orme, 1997; Krishnan and Loth, 2015). Five distinct collision outcome regimes were reported: slow coalescence, bouncing, fast coalescence, reflexive separation (i.e., the droplets rebound after temporary coalescence caused by a head-on collision), and stretching separation (i.e., the droplets stretch and then separate due to the off-center collision), the reader is referred to FIG. 4 to distinguish between the collision outcomes. These regimes are mapped in the parameter space of the impact parameter ( $B$ ) and Weber number ( $We$ ), as shown in FIG. 1. The impact parameter is the normal distance ( $b$ ) from the center of one of the colliding droplets to the vector of the relative velocity that is plotted from the center of the other droplet, normalized by the sum of the two droplets radii,

$$B = \frac{2b}{d_s + d_l}, \quad (1)$$

as sketched in FIG. 2. Where,  $d_s$  and  $d_l$  are the colliding droplets' diameters. Therefore,  $B$  has a value between 1 and 0, where 1 indicates a grazing collision and 0 a head-on collision. The Weber number is the ratio of the kinetic energy, based on the relative velocity, to the droplet surface energy,

$$We = \frac{\rho u_r^2 d_s}{\sigma}. \quad (2)$$

$\rho$  and  $\sigma$  are the droplet fluid density and surface tension, respectively.  $d_s$  and  $u_r$  are the small droplet diameter and the collision relative velocity.

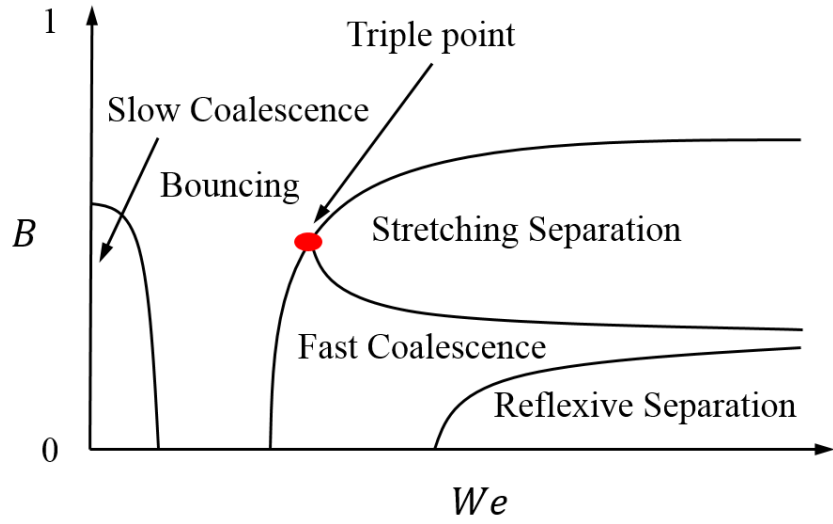


FIG. 1. A schematic of a typical regime map.

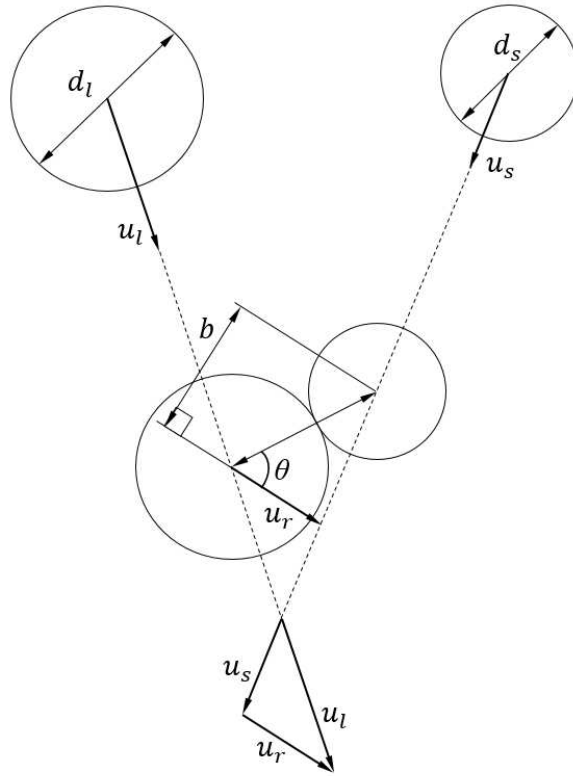


FIG. 2. Schematic of the geometry of droplet collisions.

In FIG. 1 there are four transitional boundaries separating the five regimes: slow coalescence (i.e., between slow coalescence and bouncing regimes), bouncing (i.e., between bouncing and fast coalescence regimes below the triple point, and continues above the triple point between bouncing and stretching separation regimes), stretching separation (i.e., between fast coalescence and stretching separation regimes), and reflexive separation (i.e., between fast coalescence and reflexive

separation regimes). There were many attempts to model these different transitional boundaries. Ashgriz and Poo (1990) studied the effect of the size ratio on water droplet collisions and derived two models to evaluate the boundaries of stretching separation and of the reflexive separation. Although the models consider the effect of the size ratio, they were for inviscid droplets. Later on, Jiang et al. (1992) developed a model for the stretching separation boundary in which the viscosity effect was explicitly involved in a form of two parameters. To the best knowledge of the authors, there has not been a complete reflexive separation model considering the viscous dissipation. Nevertheless, Qian and Law (1997) reported that the onset of the reflexive separation at head-on collision can be correlated with Ohnesorge number ( $Oh = \mu/\sqrt{\rho\sigma d_s}$ ); where,  $\mu$  is the dynamic viscosity of the droplet.  $Oh$  number is the ratio of the viscous energy to the surface energy. Gotaas et al. (2007b) used the approach of Qian and Law (1997) to correlate the onset of the reflexive separation with a wide range of viscosities (1-50 mPa s). Although Qian and Law (1997) and Gotaas et al. (2007b) were able to correlate the onset of the reflexive separation to  $Oh$  number which allows consideration of the viscosity effect, the size ratio of the colliding droplet was not considered. Tang et al. (2012) provided a more detailed model for the onset of the reflexive separation taking into account both the effect of viscosity and size ratio. The modelling of the slow coalescence boundary has received less attention due to the difficulties of colliding droplets at very low  $We$ . Bouncing modelling was conducted by Estrade et al. (1999) who developed a model for the lower boundary of the bouncing regime based on ethanol droplet collisions data at different size ratios. The model includes, a shape factor that can be used as a parameter to fit the data.

Kuschel and Sommerfeld (2013) conducted extensive experimental work for solutions with different solid content and thereby different viscosities to investigate the role of viscosity. The authors reported that the stretching separation and the reflexive separation regimes are shifted toward higher Weber Numbers by increasing the viscosity. Therefore, the inviscid models of Ashgriz and Poo (1990) are not adequate for high viscosity droplet collisions, while the Jiang et al. (1992) model was able to predict the boundary of the stretching separation region by adapting the viscous loss parameters in the model to fit the experimental data. Sommerfeld and Kuschel (2016) further extended the study of Kuschel and Sommerfeld (2013) by conducting more experiments on pure liquids. The authors were able to correlate the critical  $We$  of the onset of the reflexive separation (at  $B = 0$ ) for different viscosities with the Capillary number, which is the ratio of the viscous forces to the surface tension forces ( $Ca = u_r \mu/\sigma$ ). The difference between the value of the onset of reflexive separation of water and this critical  $We$  is then used to shift the boundary curve from the model of Ashgriz and Poo (1990) toward higher  $We$ . This approach successfully predicted the transitional boundary of reflexive separation region. Sommerfeld and Kuschel (2016) also discussed the model of Jiang et al. (1992) for the

stretching separation boundary and mentioned that the adapted values of the two parameters in this model can be correlated with a normalized relaxation velocity ( $u_{relax} = \sigma/\mu$ ).

On the other hand, the modelling of the lower boundary of the bouncing regime has received less attention in comparison with the modelling of the other boundaries. Sommerfeld and Kuschel (2016); Kuschel and Sommerfeld (2013); Sommerfeld and Lain (2017) reported that the model of Estrade et al. (1999) can reasonably predict the lower boundary of the bouncing regime above the triple point by adapting the shape factor to let the curve fit the experimental data. However, the model fails to predict the boundaries below the triple point. The only attempt to modify this model was by Hu et al. (2017) who altered the considered kinetic energy, which will be explained later in section IV, and added a viscous loss term. However, the performance of this model was only validated against simulation data of alumina droplets

In this paper, new experimental regime maps of binary droplet collisions of 2%, 4%, and 8% HPMC will be reported to examine the effect of the viscosity. The collisions are restricted to identical droplets size at room conditions. The three different concentrations have different viscosities, so this paper shows the effect of the viscosity on the regime maps. In addition, the modelling of bouncing regime will be discussed in detail. This will be through examining the performance of the existing models and defining the neglected physics that undermine the performance of the models. Finally, we propose a modified model to predict the boundary of the bouncing regime. It should be noted that, the models of the other regime boundaries are not considered in this study as the aim of this paper is to shed the light on the bouncing regime.

## II. THEORY OF BOUNCING

In this section, the theory of bouncing will be explored based on what have been reported in the previous studies of binary droplets collisions. The theory provides a simple background, about bouncing phenomenon of binary droplets collisions, which helps to understand the logic behind the assumptions of bouncing modelling that will be explained in sections IV and V.

The phenomenon of droplet bouncing has been widely studied experimentally and numerically. Bouncing occurs at a critical impact kinetic energy range, above and below which merging occurs (Qian and Law, 1997; Tang et al., 2012). This is widely attributed to the presence of an air layer between the two colliding droplets (Orme, 1997). At low impact velocity the air has sufficient time to be discharged. However, if the velocity is increased the air will be trapped between the two droplets and hence the droplets deform. A flattened interface will be formed between the two droplets, which causes pressure to build up in the air layer that prevents droplets from merging. This leads to consumption

of the impact kinetic energy by the deformation of the droplets, as it will be converted into surface energy and internal flow that relaxes later by the effect of the viscous dissipation. Once the impact kinetic energy vanished, bouncing occurs by the action of the surface tension which tends to recover the spherical shape to minimize the surface energy. Further increasing the impact velocity forces the air layer to be discharged and rupture the interface and therefore merging with large deformation would occur (fast coalescence).

Apart from the impact velocity, the bouncing regime was found to depend on the material of the droplets and the surrounding gas. For example, at atmospheric pressure hydrocarbon droplets show bouncing at the entire range of the impact parameter, whilst water shows bouncing only at high values of impact parameter. In addition, milk droplets show no bouncing at the entire range of impact parameter (Finotello et al., 2018). The merging of two droplets was attributed to van der Waals forces (Zhang and Law, 2011; Pan et al., 2008). However, the thickness of the air layer between the colliding droplets should be small enough for the van der Waals forces to be effective. Therefore, the difference in the bouncing observation could be more related to the difference in molecular dynamics at the surface of the droplets of different liquids. In addition, changing the conditions of the surrounding gas shows a noticeable effect on the collision outcome (Krishnan and Loth, 2015; Qian and Law, 1997). Increasing the gas pressure, density or molecular weight would promote the bouncing regime. However the presence of the droplet's liquid vapor in the surrounding gas would promote the coalescence regime (Qian and Law, 1997). All that makes it difficult to define a bouncing criteria that allows to distinguish between bouncing and coalescence based on the impact details such as  $We$  and  $B$ .

### III. EXPERIMENTAL METHODS

#### A. The apparatus

The experimental setup is illustrated in FIG. 3. It consists of two custom-made monodisperse nozzles, two high pressure syringe pumps, a high-speed camera (Photron mini AX100), a camera (acA1300-200um - Basler ace), two strobe lights, two function generators, a pulse generator and two amplifiers. The fluid is driven by the syringe pumps to the nozzles to create a continuous jet. Two square wave signals are programmed in the function generator and sent via 20X amplifier (PiezoDrive PDU150CL) to a piezo chip that is built into the nozzle. The piezo provides the required vibration to excite the jet and hence break it up into a reproducible droplet stream. By directing the nozzles towards each other in a given angle via micro rotation stages (a compact 360° rotation platform), the two droplet streams

collide. The bases of the nozzles posts have XYZR micro traversers, which allow the alignment of the droplet streams to be collided in the same plane. The side industrial camera that is attached to a microscopic lens is used to make sure that droplet streams collide in the same plane. The maximum frame rate of this camera is 200 fps; therefore, it is used with a strobe illumination source in order to freeze the movement of the droplet streams. This is done by synchronizing the pulse generator, which controls the strobe light, with one of the nozzles via the function generator. The collision outcome is recorded using the high-speed camera at 30000 fps, which allows 256 x 384 pixel in the Field of View (FOV). The high-speed camera is synchronized with another strobe light via the other function generator. This puts more control on the exposure time as the strobe light can provide 10 ns pulse duration. However, images with less light reflection were obtained at 3  $\mu$ s of light pulse duration.

The high-speed camera was attached to a Navitar microscopic zoom lens by which magnification can be controlled. However, although we can decrease the number of microns per pixel by zooming in, this would reduce the FOV. A 15  $\mu$ m/pixel was selected as balance between resolution and FOV for the droplet size in this study. Based on this resolution, the measurement of the droplet size has an uncertainty of  $\pm$  4%.

In this work, dispensing tips of gauge 30 (ID=152  $\mu$ m) were attached to the nozzles. This dispensing tip size produces droplets diameter of 360-390  $\mu$ m depending on the jet flow rate and the physical properties of the fluid; data on droplets size variation due to frequency change are provided in the Supplemental Material. The flow rate range used is 2.5-6 ml/min. The applied frequency in the nozzles ranged from 1.5-1.85 KHz depending on the jet flow rate and the physical properties. The impact parameter was controlled by using the aliasing method of Gotaas et al. (2007a). This was done by applying a frequency shift of 3 Hz, between the two nozzles, which leads to periodically sweeping the impact parameter between 1 and 0. The  $We$  number is varied by changing the angle between the two streams as wider angle produces higher relative velocity ( $u_r$ ) and hence higher  $We$ . Four regimes were produced in this study, bouncing, fast coalescence, reflexive separation and stretching separation as shown in FIG. 4. The slow coalescence regime was not considered in this study due to the instability of the jet break-up at low values of  $We$ .

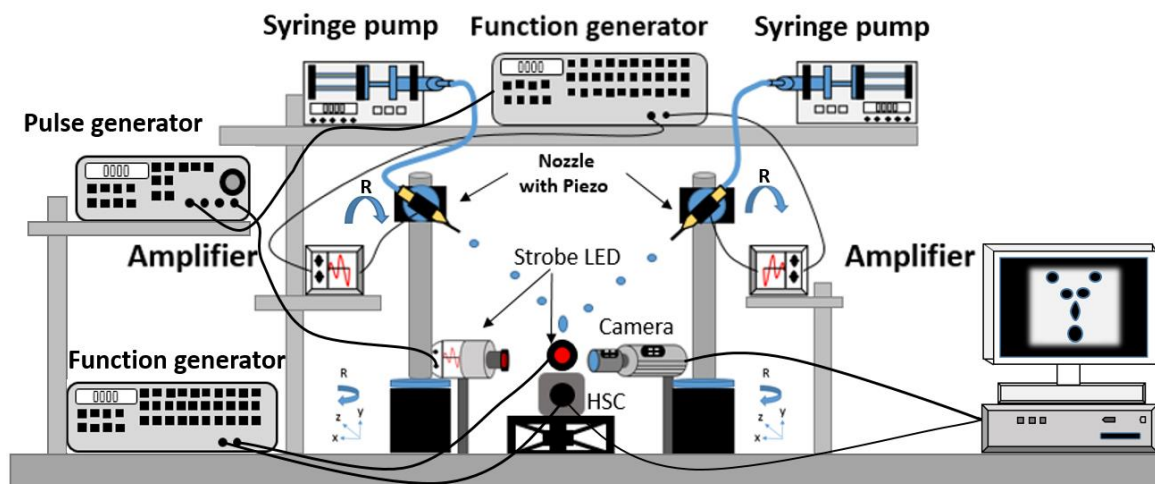


FIG. 3. Droplet collisions rig.

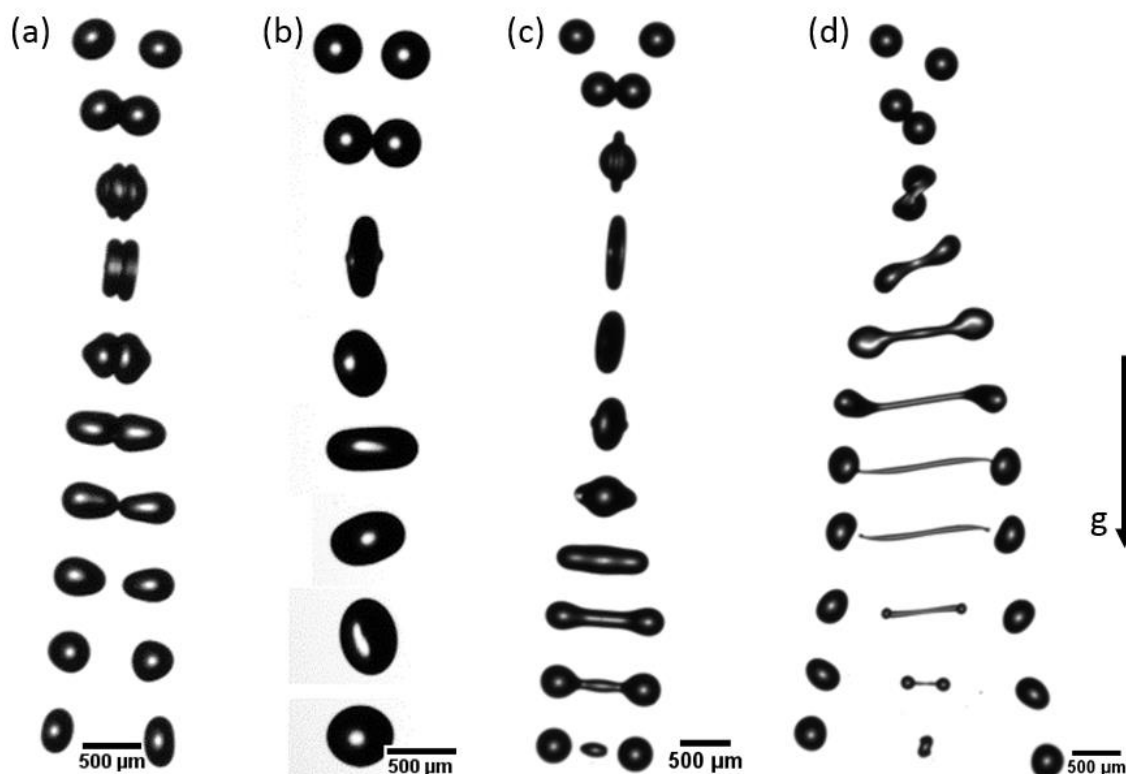


FIG. 4. Four different collisions outcomes of 2% HPMC droplets collisions, bouncing (a), fast coalescence (b), reflexive separation (c) and stretching separation (d).

### B. Droplet fluids

Three different concentrations, 2%, 4%, and 8%, of Hydroxypropyl Methylcellulose grade 603 Shin-Etsu Chemical's PHARMACOAT® (HPMC) solutions, in deionised water, were used for this study. The viscosities of the solutions were measured in a Rheometer (Bohlin Gemini) by using a cone and plate geometry and shear rate range from 1 to  $270 \text{ s}^{-1}$ . The solutions exhibit a Newtonian behaviour within the aforementioned shear rate. The surface tension was measured using a pendent drop in an optical

tensiometer (KSV CAM 200). The density was measured by weighting 50 ml of the solution using an analytical balance. Table I illustrates the physical properties of the three solutions. The measured values agree with the values that have been reported in the literature (Parker et al., 1991; Kokubo and Obara, 2008). All collisions experiments and measurements carried at atmospheric conditions and room temperature 20 °

TABLE I. Physical properties of the three HPMC systems that are used in this work.

Type of liquid	$\rho$ (kg m <sup>-3</sup> )	$\sigma$ (mN m <sup>-1</sup> )	$\mu$ (mPa s)	$Oh$ (-)
2% HPMC	998	46	2.8	0.021
4% HPMC	998	45.8	8.2	0.063
8% HPMC	997	45.7	28.4	0.216

### C. Tracking methodology

A tracking algorithm was developed to obtain the impact details from the recorded videos. the tracking algorithm is implemented by using a MATLAB based tracking software, called Droplet Morphometry and Velocimetry (DMV) that was developed by Basu (2013), to track droplets before the collision point. For each droplet, DMV provides the XY positions of droplet center, XY velocities, equivalent diameter, time, frame number, and droplet ID (as a number). Based on this data provided by DMV, the impact details are then extended with very small increments to the exact collision point using a MATLAB code that was developed by the author. The impact parameter and  $We$  are then evaluated at the collision point. The advantage of this method is to avoid cases when the exact collision point does not appear in the recording (i.e. occurred in an instance between two consequent frames), especially at high  $We$ . It should be noted that the use of the MATLAB code alongside with DMV is essential, because the latter is not designed to estimate the impact parameter. More details on the tracking methodology can be found in Appendix A.

## IV. CURRENT MODELS FOR THE BOUNCING REGIME BOUNDARY

Estrade et al. (1999) model for the bouncing regime boundary is based on an energy criterion. It states that bouncing occurs if the component of kinetic energy that contributes to the deformation of the droplets is less than the increase in surface energy required to reach the limit of maximum deformation. However, if this kinetic energy exceeds the maximum deformation limit, merging is

assumed to occur. A number of assumptions are made to derive this criterion and the subsequent equation for the boundary, these are detailed in Table II.

Applying the assumptions 1 and 2 in Table II an energy balance can be written between the system energy just prior to collision and at the point of maximum deformation

$$E_{C_e} + E_{C_d} + E_{S_i} = E_{S_f} + E_{rot}. \quad (3)$$

Where,  $E_{C_e}$  is the part of the droplet kinetic energy that does not contribute to the deformation,  $E_{C_d}$  is the kinetic energy that contributes to the deformation,  $E_{S_i}$  is surface energy of the droplets before the collision,  $E_{S_f}$  is surface energy of the droplets at the maximum deformation, and  $E_{rot}$  is the rotational kinetic energy.

TABLE II. Assumptions that Estrade et al. (1999) made to develop the bouncing model.

Assumptions	Justifications
1- No viscous loss is considered; hence all the dissipated kinetic energy is converted into surface energy.	The model was derived for inviscid droplet collisions.
2- No work against air.	No noticeable delay time was noticed before the threshold of the deformation.
3- Shape factor is fixed for the entire impact parameter range.	The regime maps of inviscid droplets exhibit bouncing boundary that fall in a narrow range of high impact parameter values.
4- The deformation is caused by the kinetic energy of the interaction region only (see FIG. 5).	The non-interacted regions have less deformation.
5- The rotational energy at the point of maximum deformation is equal to the initial energy of the non-interacting portion of the droplets, <i>i.e.</i> $E_{C_e} = E_{rot}$ .	Rotational movement at the instant of collision was noticed.

Applying assumption 4, the kinetic energy that contributes to the deformation is that of the interacting volumes shown in FIG. 5 and is given by

$$E_{C_d} = \frac{1}{2} \rho V_l (u_r \cos \theta)^2. \quad (4)$$

Where  $V_l$  is the volume of the interaction region, which is given by

$$V_l = X_l \frac{\pi d_l^3}{6} \quad (5)$$

Where  $X_l$  is the ratio of the interaction region volume, of the large droplet, to the total droplet volume, and it can be given by

$$X_l = \begin{cases} 1 - \frac{1}{4}(2 - \tau)^2(1 + \tau) & \text{for } h > \frac{d_l}{2} \\ \frac{1}{4}\tau^2(3 - \tau) & \text{for } h \leq \frac{d_l}{2} \end{cases} \quad (6)$$

$\tau$  in Eq. (6) is defined by

$$\tau = (1 - B)(1 + \Delta). \quad (7)$$

Where,  $\Delta = d_s/d_l$  is the size ratio, and

$$h = \frac{1}{2}(d_l + d_s)(1 - B). \quad (8)$$

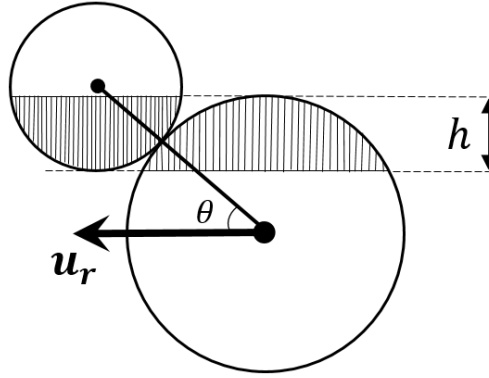


FIG. 5. A schematic representation of the interaction regions (in grey).

The surface energy of a droplet is the production of the surface tension and the droplet surface area. Thus, the total surface energy of the droplets before the collision is given by

$$E_{S_i} = \pi\sigma(d_s^2 + d_l^2). \quad (9)$$

The droplets reach the maximum deformation limit just before bouncing separation, i.e. when the kinetic energy of the interaction regions (Eq. (4)) is completely converted into surface energy (assumptions 1 and 2). Estrade et al. (1999) described the surface energy at the maximum deformation by

$$E_{S_f} = \pi\sigma d_l^2 \phi'(1 + \Delta^2). \quad (10)$$

Where,  $\phi'$  is a shape factor that is given by

$$\phi' = \frac{2}{3} \left( \frac{3}{\phi^2} + 1 \right)^{-\frac{2}{3}} + \frac{1}{3} \left( \frac{3}{\phi^2} + 1 \right)^{\frac{1}{3}}. \quad (11)$$

Estrade et al. (1999) reported that in case of collisions between unequal size droplets the shape factor can be either calculated based on the small droplets,  $\phi = h_s/r_s$  or it can be based on the large droplet,  $\phi = h_l/r_l$ , see FIG. 6.

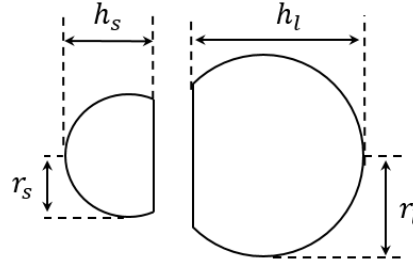


FIG. 6. Droplet shape at the instance of maximum deformation according to Estrade et al. (1999).

Substituting Eq. (4), Eq. (9), and Eq. (10), in Eq. (3) and applying assumption 5 with rearrangement gives

$$We_c = \frac{12\Delta(1 + \Delta^2)(\phi' - 1)}{X_1(1 - B^2)}, \quad (12)$$

which is the critical  $We$  that describe the boundary of the bouncing regime as a function of  $B$ .

Hu et al. (2017) extended the model of Estrade et al. (1999) to higher viscosity systems, by considering the viscous dissipation within the droplet  $E_v$ . Thus, the energy balance becomes

$$E_{C_e} + E_{C_d} + E_{S_i} = E_{S_f} + E_{rot} + E_v. \quad (13)$$

The viscous dissipation was considered a fixed percentage (independent of  $B$ ) of the kinetic energy that contributes to the deformation. Thus, Eq. (13) becomes

$$E_{C_e} + E_{C_d} + E_{S_i} = E_{S_f} + E_{rot} + \alpha E_{C_d}. \quad (14)$$

Moreover, Hu et al. (2017) used a different approach in defining the kinetic energy that contributes to the deformation, as given by

$$E_{C_d} = \frac{1}{2}\rho \left( \frac{1}{6}\pi d_s^3(u_s \cos \theta)^2 + \frac{1}{6}\pi d_l^3(u_l \cos \theta)^2 \right). \quad (15)$$

Where,  $u_s = u_r/(1 + \Delta^3)$  and  $u_l = \Delta^3 u_r/(1 + \Delta^3)$ . Importantly, Eq. (15) considers the entire droplet volume, instead of just the interaction regions.

Substituting Eq. (15), Eq. (9), and Eq. (10), in Eq. (14), as well as applying assumption 5, gives the model of Hu et al. (2017), which predicts the critical  $We$  of the lower boundary of the bouncing regime as a function of  $B$ :

$$We_c = \frac{12(1 + \Delta^3)(1 + \Delta^2)(\phi' - 1)}{\Delta^2(1 - \alpha)(1 - B^2)}. \quad (16)$$

It should be noted that Estrade et al. (1999) and Hu et al. (2017) have different definition to the kinetic energy that contributes to the deformation at head-on collisions (i.e. where both models use the entire mass of the droplets in  $E_{cd}$ ) Eq. (4) and Eq. (15), respectively. As Estrade et al. (1999) approach assumes one droplet is not moving while the other approaching at the relative velocity. Whereas, Hu et al. (2017) considers the movement of both droplets. This will be investigated in further details in section V.B.1.a.

## V. RESULTS AND DISCUSSION

### A. HPMC regime maps

The regime maps of 2% HPMC, 4% HPMC, and 8% HPMC are shown in FIG. 7. The expect regimes were seen and their overall shapes are consistent with previous work, for instance (Qian and Law, 1997; Kuschel and Sommerfeld, 2013). The Figures clearly show that the reflexive separation boundary is shifted toward higher  $We$  by increasing the viscosity. The reflexive separation regime disappeared at 8% HPMC for the investigated range of  $We$ . That qualitative trend of the viscosity effect agrees with the previous studies of Kuschel and Sommerfeld (2013); Sommerfeld and Kuschel (2016); Gotaas et al. (2007b); Finotello et al. (2018); Finotello et al. (2017), where more details about these trends can be found.

The regime maps also show that as the viscosity increases the bouncing regime boundary shifts toward lower  $We$ . This might be because at higher viscosity, more kinetic energy is viscously dissipated and hence less energy is converted into surface energy. This results in less deformation and consequently less trapped air between the droplets which can be easily discharged to promote the coalescence regime.

In the following sections, the modelling of the bouncing boundary will be discussed by assessing the existing models and proposing a new model. In FIG. 7 the solid black curve is fitted manually to the bouncing boundaries of the three HPMC systems. This curve will be used as reference in the oncoming discussion to allow for removing the data points and reducing the noise in the Figures. It should be noted that a detail analysis of the other regime boundaries is not within the scope of this paper.

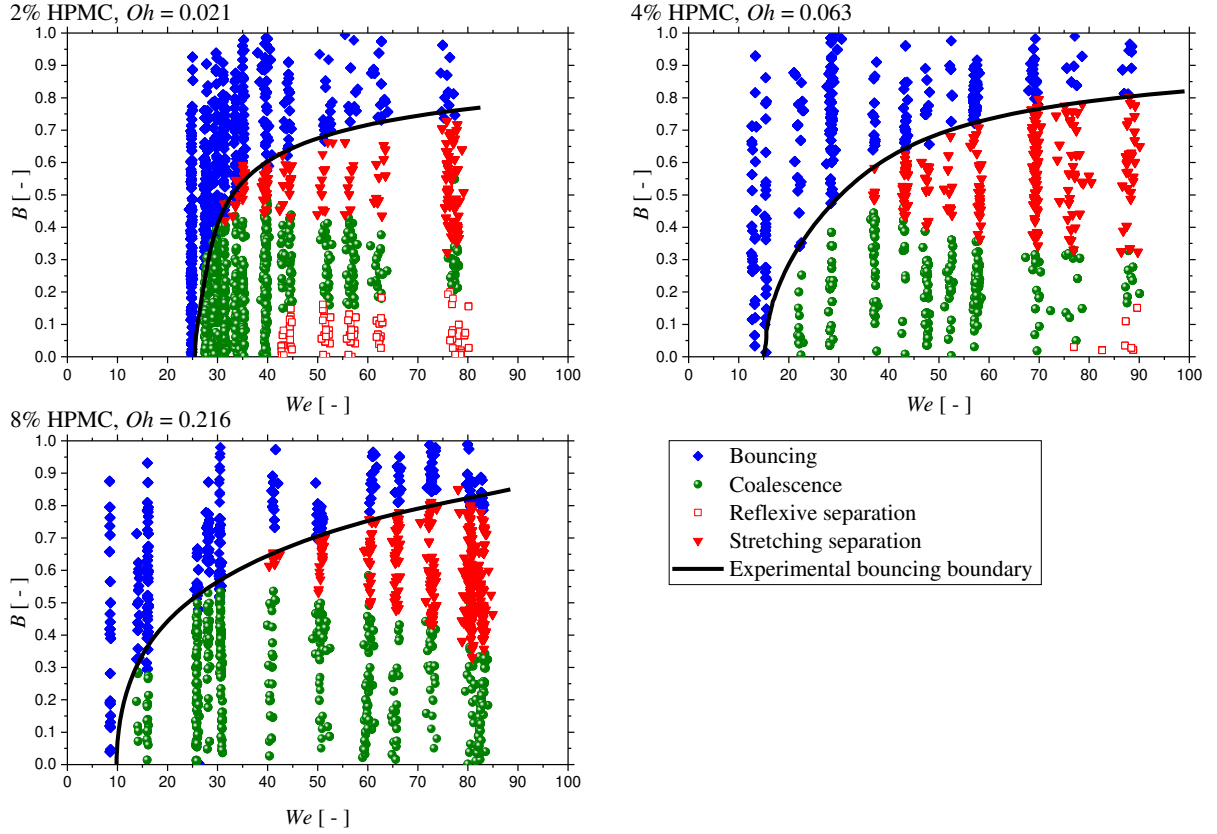


FIG. 7. HPMC regime maps for the three concentrations 2%, 4%, and 8%.

## B. Assessment of the existing bouncing models

To assess the performance of the models of Estrade et al. (1999) and Hu et al. (2017) a line defining the boundary of the bouncing regime was manually fitted to the experimental data, see FIG. 7. This curve was digitized using Origin 2017 with a  $B$  increment of 0.01. These data points were used to optimize the shape factor  $\phi'$  by minimizing the Mean Absolute Error:

$$\text{MAE} = \frac{1}{n} \sum_{i=1}^n |We_{model} - We_{exp.}|_i. \quad (17)$$

The use of the MAE quantitatively characterizes the performance of the models. The viscous dissipation parameter in Hu et al. (2017) model was set as 0.5 for the three HPMC solutions. This value was used as an approximation based on the numerical simulation of Xia and Hu (2014) who reported that the viscous loss of alumina droplets that has viscosity 14 mPa.s is approximately 50% of the kinetic energy.

FIG. 8 clearly reveals that the models of Estrade et al. (1999) and Hu et al. (2017) are not adequate to predict the boundary of bouncing regime for all range of  $B$ . However, plotting them with different viscosities would be helpful to theoretically analyzing their limitations, as will be shown in the following discussion.

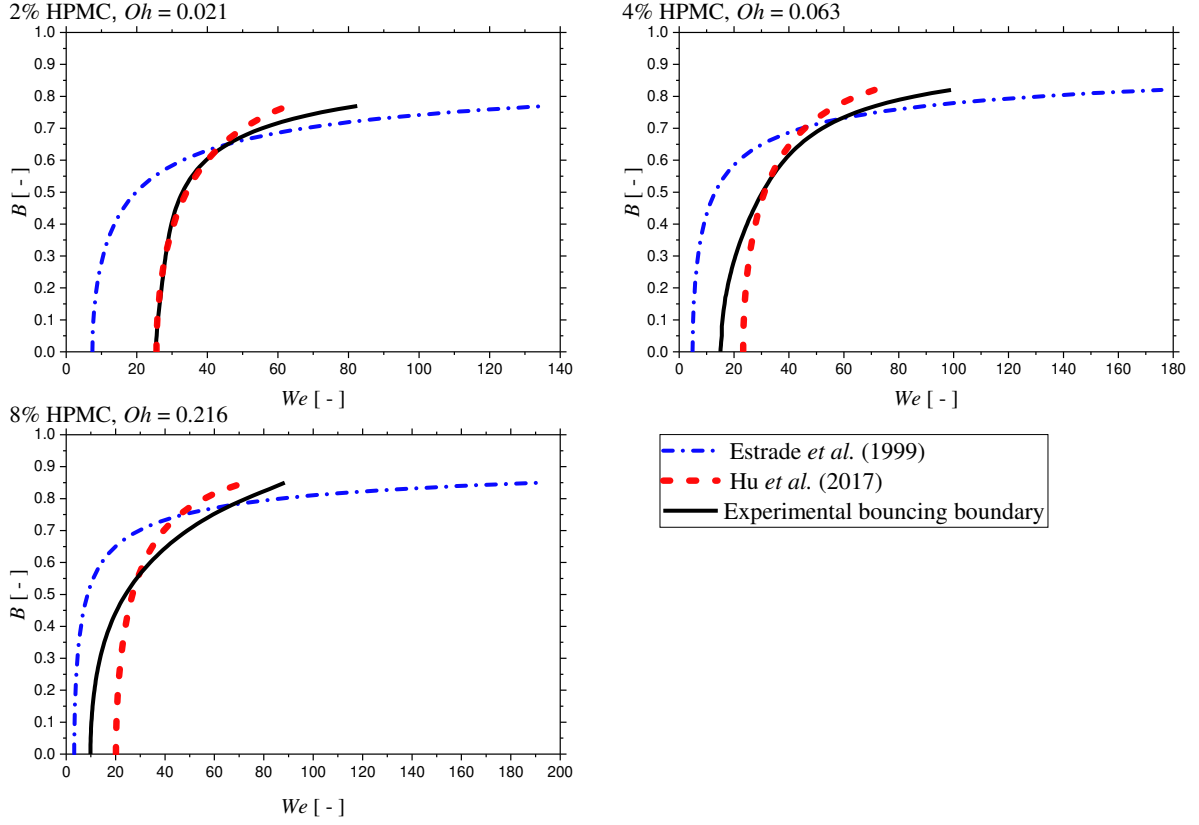


FIG. 8. The performance of Estrade et al. (1999) model in Eq. (12) and Hu et al. (2017) model in Eq. (16) on the HPMC regime maps for the three concentrations that used in this work, 2%, 4%, and 8%.

TABLE III. A quantitative summary of the performance of the models of Estrade et al. (1999) and Hu et al. (2017).

	Estrade et al. (1999) Eq. (12)		Hu et al. (2017) Eq. (16)		
	$\phi'$	MAE	$\phi'$	$\alpha$	MAE
2% HPMC	1.31	16.05	1.27	0.50	1.77
4% HPMC	1.21	15.18	1.24	0.50	6.10
8% HPMC	1.14	14.63	1.21	0.50	8.35

Table III, shows an overall improvement in the prediction when Hu et al. (2017) model is used where the MAE remains in the range of 1.74 to 8.35 for the three systems, whereas, Estrade et al. (1999) model shows MAEs in the range of 14.63 to 16.05. It can also be noticed from Table III and FIG. 8 that Estrade et al. (1999) model shows an increasing accuracy as the viscosity increases, as the MAE was reduced from 16.05 in 2% HPMC to 14.63 in 8% HPMC. In contrast, Hu et al. (2017) model exhibits an opposite behavior, where the MAE increased from 1.74 in 2% HPMC to 8.35 in 8% HPMC, respectively. Moreover, qualitatively, for the three systems the model of Estrade et al. (1999) could not follow the

trend of the experimental boundary starting from under-prediction of  $We_c$  at low  $B$  and crosses the experimental curve above the triple point to over-prediction of  $We_c$  at high  $B$ . However, the boundary predicted by the model of Hu et al. (2017) crosses the experimentally observed boundary near the triple point, especially in the cases of 4% and 8% HPMC, by over-predicting  $We_c$  at low  $B$  and under-predicting  $We_c$  at high  $B$ . The following paragraphs explain the reasons behind these observations.

In both models it is assumed that the maximum deformation limit is independent of the impact parameter (i.e. constant shape factor, assumption 3 in Table II). However, the maximum deformation limit decreases significantly as the impact parameter increases, as can be seen in case of 2% HPMC in FIG. 9. Consequently, an over-prediction of  $We_c$  would be expected at high  $B$  values if the model is fitted to the experimental  $We_c$  at  $B=0$ , as shown in FIG. 10. This explains the trend of the model of Estrade et al. (1999) in FIG. 8, as the minimum MAE fits the model at a  $B$  value near the triple point (the cross point). This means the selected  $\phi'$  value produces less surface area at the maximum deformation limit than that at near head-on collisions and thereby under-prediction of  $We_c$  below the cross point and higher than that at high  $B$  values above the cross point which cause the over-prediction of  $We_c$ .

However, Hu et al. (2017) et al. (2017) shows an under-prediction of  $We_c$  at high values of  $B$  when the model fits the experimental boundary at  $B=0$ , as shown in FIG. 10. This trend is contrary to expectations due to the constant shape factor assumption. This can be explained by the overestimation of kinetic energy, at high  $B$  values, that is considered by using of the entire droplet mass regardless the percentage of interaction regions. The excessive kinetic energy that is considered to contribute to the deformation has an opposite effect to the constant shape factor assumption. This opposite effect reduces the impact of these assumptions on the model, which explains the overall improvement in the prediction of the model of Hu et al. (2017) compared to the model of Estrade et al. (1999). However, the excessive kinetic energy seems to have a larger impact on the curve than that of the constant shape factor assumption. This leads to an under prediction of  $We_c$  at high  $B$  values when the model is fitted to the experiments at head-on collisions, as shown in FIG. 10. That explains the trend of the model of Hu et al. (2017) in FIG. 8, as the Minimum MAE selects  $\phi'$  value that fits the model at a cross point near the triple point and thereby an under-prediction of  $We_c$  above this point and an over-prediction of  $We_c$  below it.

The case of 8% HPMC in FIG. 9 shows that at high viscosity, the assumption of constant shape factor has less significance in comparison to the case of 2% HPMC. This because that the bouncing boundary occur at low  $We_c$  and hence at low kinetic energy. Due to the high viscosity, significant amount of this kinetic energy would be dissipated. Consequently, less Kinetic energy will be transformed into surface

energy and hence low deformation occurs at low  $B$ , which makes the shape factor more comparable with that at higher  $B$  values in comparison to the bouncing of lower viscosity droplets. Therefore, the prediction accuracy increases with the increase of the viscosity by using the model of Estrade et al. (1999). However, the accuracy of the model of Hu et al. (2017) decreases by increasing the viscosity as the opposite effect of the constant shape factor to the effect of the excessive kinetic energy is lower than that at low viscosity.

Although Estrade et al. (1999) and Hu et al. (2017) have different definition to the kinetic energy that contributes to the deformation at head-on collisions, this should not affect the above discussion as both models are optimized by fitting the shape factor for the minimum MAE. This means any difference due to the difference in the kinetic energy will be recovered by the fitted shape factor. Similarly, the existence of the viscos loss term in the model of Hu et al. (2017) should not affect the discussion. Ultimately, the difference in the shape of the two models is due that Estrade et al. (1999) consider the mass of the interaction regions in the kinetic energy that contributes to the deformation while Hu et al. (2017) consider the entire mass; this cannot be recovered by the fitted shape factor because  $X$  is a function of  $B$  while the shape factor is not.

From the discussion in this section, an accurate model that can evaluate the boundary of the bounding regime requires, a shape factor that accurately reflexes the geometry of the droplet at maximum deformation, correct definition of the kinetic energy that contributes to the deformation, good estimation to the viscous losses, and implementing the effect of the impact parameter on the shape factor and the kinetic energy that contributes to the deformation. Therefore, in the next sections, these parameters will be assessed firstly at head-on collisions then the analysis will be extended to the entire range of  $B$ .

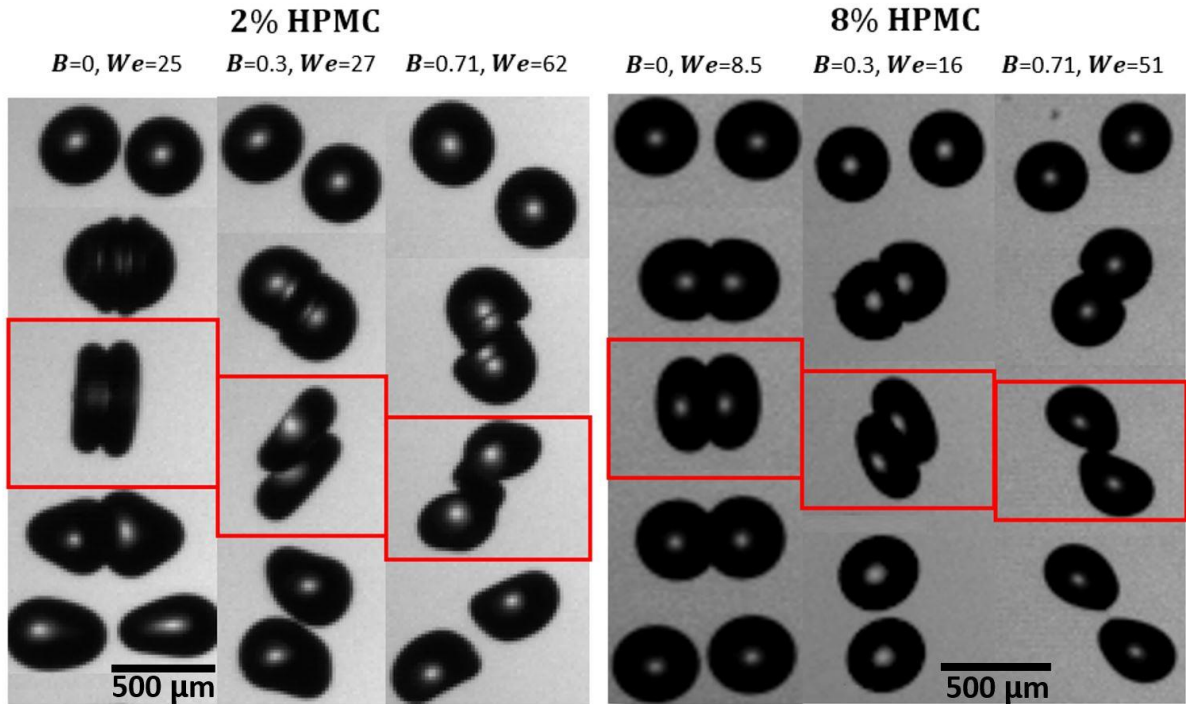


FIG. 9. The maximum deformation of 2% and 8% HPMC at different values of impact parameter for Weber numbers that occur on the boundary of the bouncing regime.

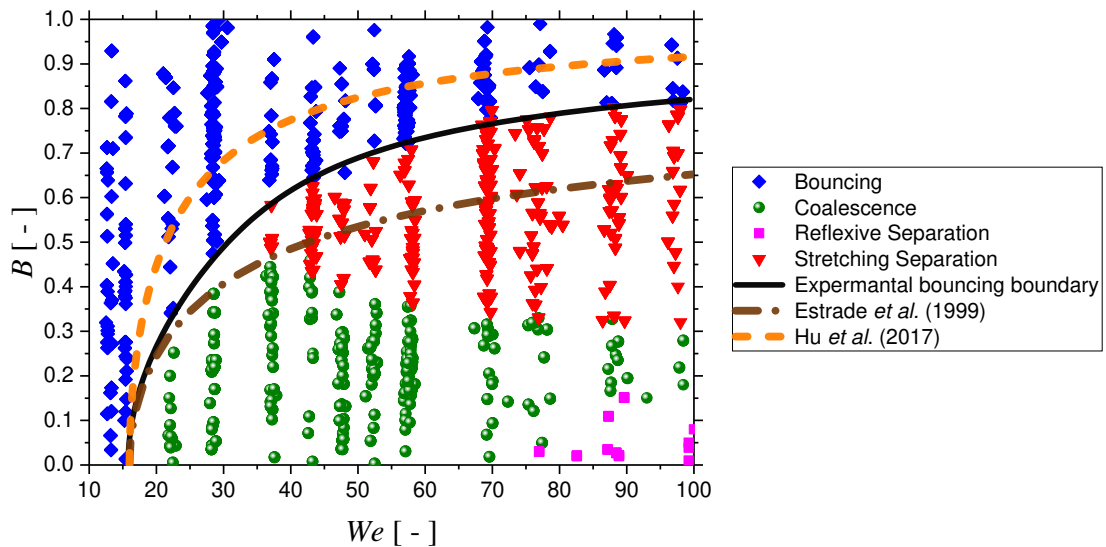


FIG. 10. The performance of the existing models when they are fitted to the onset of coalescence at head-on collisions, which show the over-prediction of the model of Estrade et al. (1999), Eq. (12), and the under-prediction of the model of Hu et al. (2017), Eq. (16) on 4% HPMC regime map.  $\phi'$  is 5.0 in the model of Estrade et al. (1999) while it is 3.5 in the model of Hu et al. (2017) and  $\alpha$  is 0.5.

## 1. Assessment of the models' parameters at head-on collisions

### a. Kinetic energy assessment

As mentioned earlier, the two models have different definition to the kinetic energy that contributes to the deformation. To assess the validity of these two different approaches, they are examined for head-on collisions, where both approaches consider the kinetic energy of the total drop mass.

The momentum of a moving droplet is given by  $P = mu$ , where  $m$  and  $u$  are mass and velocity of the droplet respectively. Therefore, the kinetic energy of the droplet is given by:

$$E_k = \frac{1}{2}uP. \quad (18)$$

This relation will show if the two approaches of the kinetic energy are conserve the momentum in a zero-momentum frame.

In head on bouncing collision of equal diameter ( $d$ ) droplets, if each droplet has a velocity equal to  $u = u_r/2$ , the total momentum of the two colliding droplets is

$$P = \frac{\pi}{6}\rho d^3 u_r \quad (19)$$

Substituting Eq. (19) in Eq. (18) gives the total kinetic energy of the droplets

$$E_k = \frac{\pi}{24}\rho d^3 u_r^2. \quad (20)$$

At head on collisions,  $X_l$  and  $\cos^2\theta$  are both equal one. Thus, the kinetic energy of the model of Estrade et al. (1999), from the combination of Eqs. (4-6), is  $E_{Cd} = (1/12)\pi\rho d^3 u_r^2$ . This reveals that Estrade et al. (1999) double the kinetic energy that contributes to the deformation by compared to Eq. (20). However, the approach of Hu et al. (2017) more universal, as simplifying Eq. (15), for head-on collisions of equal size droplets, gives  $E_{Cd} = (1/24)\rho d^3 u_r^2$ , which recovers Eq. (20). Thus, the approach of Hu et al. (2017) will be the considered in the rest of this paper.

#### *b. Shape factor assessment*

By looking at the both aforementioned models (Eq. (12) and Eq. (16)) it can be realized that the shape factor  $\phi'$  should always have a value  $>1$ , otherwise the models would produce zero or negative values of  $We_c$ . This implies that  $\phi$  must have a value that is always less than 0.40, according to Eq. (11), as shown in FIG. 11. However,  $\phi \equiv 2$  for grazing collisions ( $B=1$ ), and the direct measurement at head-on collision from the images of 2% HPMC in FIG. 9 at maximum deformation reveals that  $\phi \sim 0.648$  for 2% HPMC. This range of  $\phi$  (from 2 to 0.648) is above 0.4, which implies that the shape factor  $\phi' < 1$ , as shown in FIG. 11. Thus, this shows that the commonly used shape factors of the existing models are not seen in reality, and hence the suggested equation for the maximum deformation seems to be invalid. To verify the validity of this equation, the shape factor of spherical cup was rederived in this work, see Appendix B. The new derivation of the shape factor proved that Eq. (11) should be in the following form

$$\phi'_c = \frac{2}{3} \left( \frac{6}{\phi} - 2 \right)^{-\frac{1}{3}} + \frac{1}{3} \left( \frac{2}{\phi} - 2 \right)^{\frac{2}{3}}. \quad (21)$$

and the form of Eq. (11) is might be due to a derivation mistake by Estrade et al. (1999). Eq. (21) shows that  $\phi'_c > 1$  for the visible range of  $\phi$  (from 0 to 2), as shown in FIG. 11.

As the shape factor was corrected in Eq. (21), it would be interesting to use it, by measuring  $\phi$  from the experimental images, to evaluate the critical  $We_c$  of the onset of coalescence at head-on collisions. This by using the model of Hu et al. (2017) as it implements the correct kinetic energy as justified in the previous section. The model firstly tested without considering the viscous losses (i.e.  $\alpha = 0$ ). The model slightly over-predicts the onset of coalescence in case of 2% HPMC and gives a reasonable agreement in 4% HPMC and 8% HPMC, as illustrated in Table IV. However, adding viscous losses would further over-estimates  $We_c$ . This implies that the spherical cup geometry over-estimates the surface energy at the maximum deformation. Thus, there is a requirement for a shape factor that has a better agreement with the geometry of the droplets at the maximum deformation. Thus, a new shape factor will be proposed, in the next sub-section.

TABLE IV. Comparison between the experimental and the predicted  $We_c$  of the onset of coalescence using Eq. (16) using different shape factors (spherical cup and oblate spheroid) at  $B = 0$ , and  $\alpha = 0$ .

	Spherical cap geometry			Oblate spheroid geometry	
	$We_c$ Experimental	$\phi'_c$ Eq. (21)	$We_c$ Eq. (16)	$\phi'_{o.s.}$ Eq. (26)	$We_c$ Eq. (16)
2% HPMC	26 ± 1	1.59	28.51	1.46	22.01
4% HPMC	16 ± 3	1.33	16.05	1.24	11.45
8% HPMC	12 ± 2	1.21	10.32	1.14	6.67

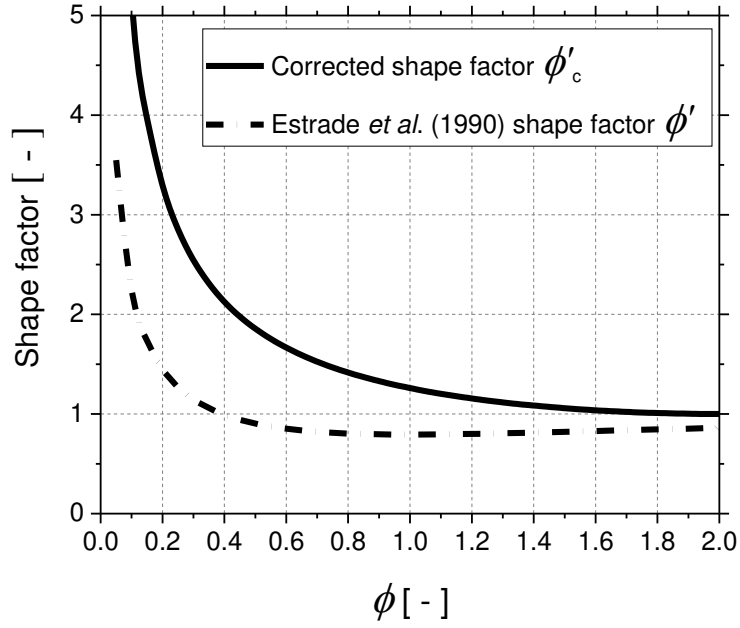


FIG. 11. The shape factor  $\phi'$  in Eq. (11) and Eq. (21) as a function of the shape parameter  $\phi$ .

*c. The proposed shape factors*

The images in FIG. 9 reveals that the maximum deformation of the droplets at head-on collisions have a shape that approximates an oblate spheroid more than spherical cup. The surface area of an oblate spheroid is given by

$$SA_{oblate} = 2\pi a^2 + \pi \frac{c^2}{e} \ln \left( \frac{1+e}{1-e} \right). \quad (22)$$

Where,  $a$  and  $c$  are shown in FIG. 12, and  $e^2 = 1 - \frac{c^2}{a^2}$ . Thus, the surface energy equation at the maximum deformation can be given by

$$E_{S_f} = 2\pi\sigma a_l^2 + \pi\sigma \frac{c_l^2}{e_l} \ln \left( \frac{1+e_l}{1-e_l} \right) + 2\pi\sigma a_s^2 + \pi\sigma \frac{c_s^2}{e_s} \ln \left( \frac{1+e_s}{1-e_s} \right), \quad (23)$$

which considers the effect of size ratio by implementing  $e_l$  and  $e_s$ . Where,  $e_l^2 = 1 - (c_l^2/a_l^2)$  and  $e_s^2 = 1 - (c_s^2/a_s^2)$ . It should be noted that  $e_l^2$  and  $e_s^2$  are expected to be unequal in case of collisions between droplets that have non-identical size. This is due to the difference in the capillary pressure ( $4\sigma/d$ ) between the droplets, as the small droplet has higher capillary pressure and hence higher resistance to the deformation. This is in contrary to the assumption of Estrade et al. (1999) that  $\phi = h_l/R_l = h_s/R_s$ .

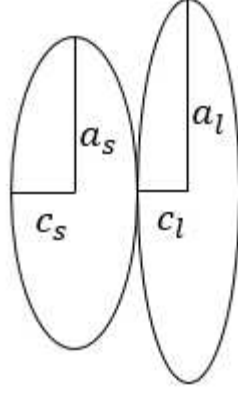


FIG. 12. The oblate spheroid shape that proposed for the maximum deformation at head-on collisions.

From mass conservation before the collision and at the maximum deformation, the volume of the oblate spheroid, given by  $V_{oblate} = (4/3)\pi a^2 c$ , is equal to a volume of a sphere, given by  $V_{sphere} = (1/6)\pi d^3$ , that has a diameter  $d$  equal to the droplet diameter before the collision.

$$4a^2 c = \frac{1}{2} d^3. \quad (24)$$

Solving Eq. (24) for  $a$ ,  $c$ , and  $d$  and substituting it in Eq. (23) gives

$$E_{S_f} = \frac{1}{2} \pi \sigma d_l^2 \left( \left( \left( \frac{1}{1-e_l} \right)^{\frac{1}{3}} + \frac{1}{2} \left( \frac{(1-e_l)^{\frac{2}{3}}}{e_l} \right) \ln \left( \frac{1+e_l}{1-e_l} \right) \right) + \Delta^2 \left( \left( \frac{1}{1-e_s} \right)^{\frac{1}{3}} + \frac{1}{2} \left( \frac{(1-e_s)^{\frac{2}{3}}}{e_s} \right) \ln \left( \frac{1+e_s}{1-e_s} \right) \right) \right). \quad (25)$$

From the analogy between Eq. (25) and Eq. (10), the shape factor of an oblate spheroid geometry ( $\phi'_{o.s.}$ ) is given by

$$\phi'_{o.s.} = \frac{1}{(2 + 2\Delta^2)} \left( \left( \left( \frac{1}{1-e_l} \right)^{\frac{1}{3}} + \frac{1}{2} \left( \frac{(1-e_l)^{\frac{2}{3}}}{e_l} \right) \ln \left( \frac{1+e_l}{1-e_l} \right) \right) + \Delta^2 \left( \left( \frac{1}{1-e_s} \right)^{\frac{1}{3}} + \frac{1}{2} \left( \frac{(1-e_s)^{\frac{2}{3}}}{e_s} \right) \ln \left( \frac{1+e_s}{1-e_s} \right) \right) \right). \quad (26)$$

Using the new shape factor of the oblate spheroid, Eq. (26), rather than the shape factor of the spherical cap, Eq. (21), with keeping  $\alpha = 0$ , results in an under-prediction of  $We_c$  for the three HPMC solutions, as shown in Table IV, which is the expected scenario due to the neglect of the viscous losses. This reveals that the oblate spheroid geometry is better in describing the geometry of the droplet at the maximum deformation, since it produces a shape factor that has a lower value than the spherical cap, as illustrated in Table IV, and hence lower surface energy at the maximum deformation.

*d. Viscous losses estimation*

The process of bouncing can be divided into two stages: the initial deformation from the time of contact,  $t_o$ , to the point of maximum deformation,  $t_{m1}$ , and a period of oscillating relaxation where the droplets return to their original spherical shape at  $t_{rn}$  as shown in FIG. 13. The total viscous dissipation in the bouncing collision process takes place during both these periods due to the induced internal flow. Assuming viscous losses are the only sources of energy loss, then the viscous energy loss,  $E_{vt}$ , is equal to the difference in the system kinetic energy before and after the head-on collision, i.e.  $E_{vt} = E_{Cd} - E_{kf}$ . Where,  $E_{kf}$  is the kinetic energy of the droplets post collision is given by  $mu_f^2$  and where  $u_f$  is the velocity of each of the rebounding droplets. This velocity can be measured by tracking the separating droplets.

The viscous loss in the bouncing model,  $E_v$  is that due to the deformation in the period from  $t_o$  to  $t_{m1}$ . Therefore, to estimate  $E_v$  it is necessary to estimate the ratio of the viscous losses during period of  $t_o - t_{m1}$  to the total viscous losses,  $E_{vt}$ . If the droplets are viscous and recovered their spherical shape without oscillation, this fraction will be  $\sim 50\%$  and hence  $\alpha \sim 0.5E_{vt}/E_{Cd}$ . This is based on the assumption that the losses during the compression period from  $t_o$  to  $t_{m1}$ , is equal relaxation period when the droplet returns to its spherical shape at  $t_{r1}$ . In the more general case when the droplets show oscillations during the relaxation period, see FIG. 14, estimating  $\alpha$  requires an estimate of the viscous losses in this period.

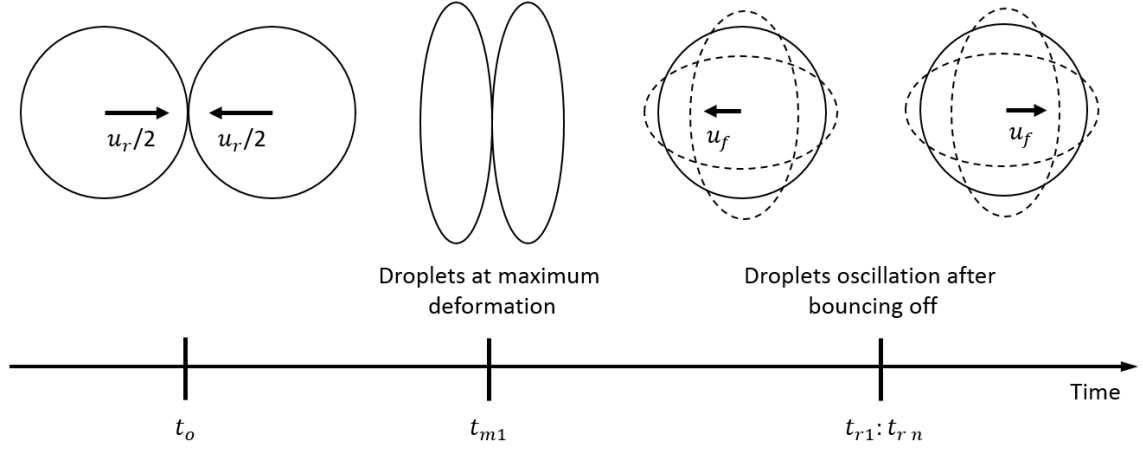


FIG. 13. The stages of bouncing process.

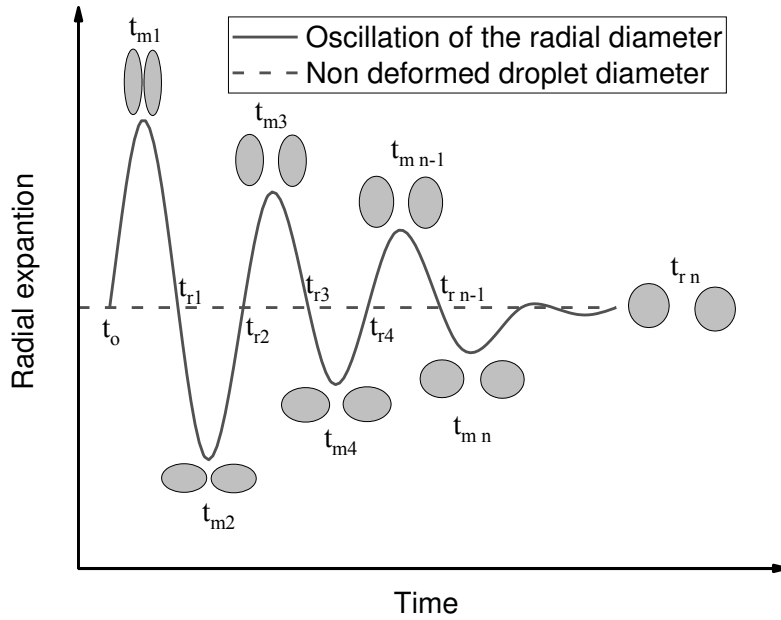


FIG. 14. The radial oscillation of the droplets during the bouncing collision.

If the assumption is made that the viscous energy loss in each overshoot is proportional to the elongation of the droplet,  $|d_r|_{t_{mi}} - d|_{t_0}|$ , then the contribution of deformation of the period  $t_{r1} - t_0$  to the total viscous losses can be approximated by

$$\frac{E_v|_{t_{r1}-t_0}}{E_v} \sim \frac{d_r|_{t_{m1}} - d|_{t_0}}{\sum_{i=1}^n |d_r|_{t_{mi}} - d|_{t_0}|}. \quad (27)$$

Where,  $d_r$  is the length of the droplet measure along its principal axis. However, the viscous loss that is considered in the bouncing model is roughly half the viscous loss in the period  $t_{r1} - t_0$ . Thus, the viscous losses factor is in the order of

$$\alpha \sim 0.5 \frac{E_v|_{t_{r1}-t_0}}{E_{cd}}. \quad (28)$$

8% HPMC shows that 88% of  $E_{cd}$  is dissipated by the total viscous losses, and no oscillation after  $t_{r1}$ , which means  $\alpha \sim 44\%$ , as shown in Table V. While, 4% HPMC shows 70% of  $E_{cd}$  is dissipated by the total viscous losses, and of one cycle after  $t_{r1}$  (i.e. reaches its final relaxation state at  $t_{r2}$ ). More oscillations were noticed in 2% HPMC, which shows six cycles after  $t_{r1}$ ; and 75% of  $E_{cd}$  is dissipated by the total viscous losses. Applying Eq. (28) to 2% HPMC and 4% HPMC gives that the viscous dissipation factor is approximately 0.11 and 0.33, respectively, as shown in Table V. Using these approximated values of  $\alpha$  in the model of Hu et al. (2017) with the measured values of the proposed shape factor Eq. (26), shows good agreement of the predicted  $We_c$  with the experiments, as shown in Table V.

TABLE V. Comparison, at head-on collisions, between the experimental and the predicted  $We_c$  of the onset of coalescence using Eq. (16) with the oblate spheroid shape factor, Eq. (26), and Eq. (28) for the viscous dissipation factor.

	$\alpha$ Eq. (28)	$\phi'_{o,s}$ Eq. (26)	$We_c$ experimental	$We_c$ Eq. (16)
2% HPMC	0.11	1.46	26 ±1	24.72
4% HPMC	0.23	1.24	16 ±3	15.8
8% HPMC	0.44	1.14	12 ±2	11.90

## 2. The effect of the impact parameter

### a. Kinetic energy assessment

As mentioned early, considering the total mass of the droplet in  $E_{cd}$  leads to under-predict  $We_c$  at high values of  $B$ . Therefore, the mass of the interaction regions should be considered in the approach of Hu et al. (2017) in evaluating the kinetic energy that contributes to the deformation. This should be considered for both small and large droplet, in case of collisions of unequal size droplets. Therefore, the equation of the kinetic energy that contributes to the deformation will be

$$E_{cd} = \frac{1}{2} \rho \left( X_l \frac{1}{6\Delta^3} \pi d_s^3 \left( \frac{\Delta^3 U_r}{1+\Delta^3} \cos \theta \right)^2 + X_s \frac{1}{6} \pi d_s^3 \left( \frac{U_r}{1+\Delta^3} \cos \theta \right)^2 \right). \quad (29)$$

Where,  $X_l$  is given by Eq. (6) and

$$X_s = \begin{cases} \left( 1 - \frac{1}{4\Delta^3} (2\Delta - \tau)^2 (\Delta + \tau) \right) & \text{for } h > \frac{d_s}{2} \\ \frac{1}{4\Delta^3} \tau^2 (3\Delta - \tau) & \text{for } h \leq \frac{d_s}{2} \end{cases}. \quad (30)$$

Where,  $\tau$  and  $h$  are defined in Eq. (7) and Eq. (8), respectively.

*b. Shape factor assessment*

As mentioned before the degree of deformation decreases with the impact parameter (i.e. decrease in the surface area at the maximum deformation), see FIG. 9. Therefore, to predict the lower boundary of the bouncing regime, for the entire range of  $B$ , the decrease in the surface area of the droplet at the maximum deformation needs to be considered. In FIG. 9, it can be noticed that the deformation has less dependency on the impact parameter at the range from 0 to 0.3 than at the range from 0.3 to 0.7, especially in case of 2% HPMC. Thus, we need to account for the non-linear decrease in shape factor see with increasing  $B$ . As the factor  $e$  is an indicator of deformation, the surface area can be correlated with  $B$  via  $e^2$  and the following power law correlation is proposed

$$e' = \sqrt{\frac{e^2}{1+\Psi B^\beta}}. \quad (31)$$

Where,  $\Psi$ , and  $\beta$  are positive constants that can be optimized to fit the data. Therefore,  $\phi''_{o.s.}$  is the new shape factor that account for the effect of  $B$ , which is similar to that in Eq. (26) but using  $e'$  instead of  $e$ . Eq. (31) allows for that at  $B = 0$ ,  $e' = e$  and hence  $\phi''_{o.s.} = \phi'_{o.s.}$ .

*c. The performance of the new model*

Using Eq. (29) and the proposed shape factor  $\phi''_{o.s.}$ , the bouncing boundary model will be

$$We_c = \frac{12\Delta^2(1+\Delta^2)(1+\Delta^3)^2(\phi''_{o.s.} - 1)}{(Xs + \Delta^3 X_D)(1-B^2)(1-\alpha)}. \quad (32)$$

Using this model, Eq. (32), with the approximated values of  $\alpha$  in section V.B.1.d., and the measured values of  $\phi''_{o.s.}$  at head-on collisions, in Table VI, and then Optimizing  $\Psi$ , and  $\beta$  instantaneously for the minimum MAE, show significant improvement in the prediction of the bouncing boundary, as shown qualitatively in FIG. 15. The proposed model shows excellent agreement with experimental data whether above or below the triple point for the three HPMC solutions. Quantitatively, Table VI shows that the MAE of the proposed model is significantly reduced compare to that of the models of Estrade et al. (1999) and Hu et al. (2017) in Table III. Compare to the model of Estrade et al. (1999), the MAE was reduced by 99%, 97%, and 87% for 2% HPMC, 4% HPMC, and 8% HPMC, respectively. And compare to the model of Hu et al. (2017), it was reduced by 87%, 93%, and 77% for 2% HPMC, 4% HPMC, and 8% HPMC, respectively.

TABLE VI. The performance of the proposed model in Eq. (32) in predicting the bouncing boundary of 2%, 4%, and 8% HPMC.

	$\alpha$ Eq. (28)	$\phi''_{o.s.}$ (at $B = 0$ )	$\Psi$	$\beta$	MAE
2% HPMC	0.11	1.46	0.86	2.75	0.23
4% HPMC	0.23	1.24	1.05	3.93	0.40
8% HPMC	0.44	1.14	1.11	4.70	1.91

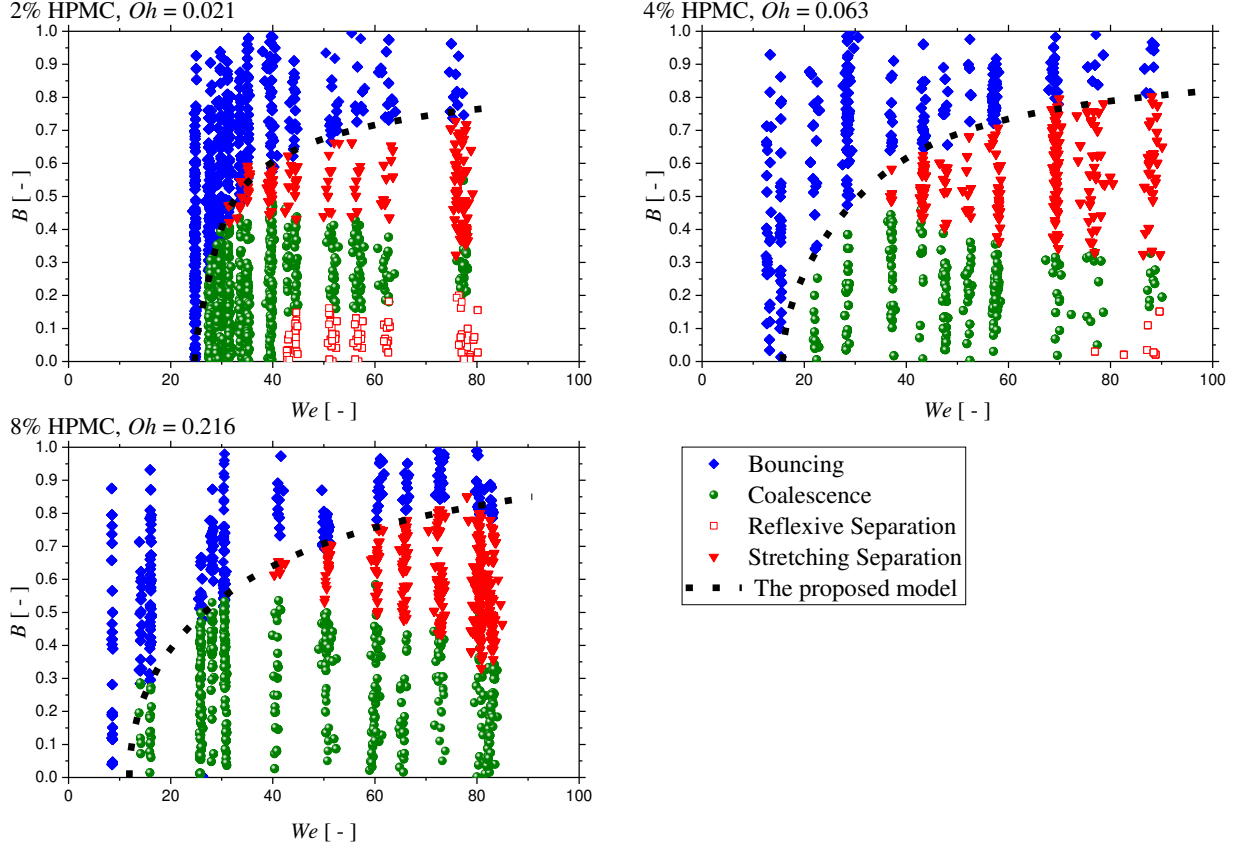


FIG. 15. The performance of the proposed model Eq. (32) compare to bouncing boundaries on the HPMC regime maps for the three concentrations, 2%, 4%, and 8% .

## VI. CONCLUSION

In this work, three novel regime maps of binary droplet collisions outcomes for three different concentrations of HPMC aqueous solution, 2%, 4%, and 8% were developed experimentally. Increasing the concentration of HPMC, increases the solution viscosity, and shifts the boundary of the separation regimes toward higher  $We$  due to the higher viscous dissipation. In, contrast the bouncing regime boundary shifted toward lower  $We$ ; because, the higher viscous dissipation reduces the deformation and hence faster air discharge between the colliding droplets.

The performance of the existing models predictions of the boundary of bouncing regime was assessed against the experimental data using the mean absolute error as a quantitative measure. Generally, the model of Hu et al. (2017) shows better accuracy than the model of Estrade et al. (1999). The poor performance of the model of Estrade et al. (1999) is primarily attributed to the assumption that the surface energy at the maximum deformation is independent of the impact parameter, i.e. constant shape factor. However, for the more viscous system studied here the experimental images clearly show that the deformation reduces significantly with the impact parameter and consequently a constant shape factor cannot be assumed. Hu's approach also assumes a constant shape factor however the inclusion of the entire droplet kinetic energy in the energy balance, in contrast to Estrade et al. (1999) who only include the interacting regions, counteracts this assumption and reduces the deviation of the model from the experimental data. (The addition of the loss factor in Hu's model does not help improve the fit as it does not change the shape of the curve.)

Several errors in the derivation of the models were also identified. The derivation of the spherical cap shape factor of Estrade et al. (1999), which was reapplied by Hu et al. (2017), was shown to contain an error. However, an oblate spheroid geometry was found to give a better fit to the droplet shape at maximum deformation for head-on collisions than the spherical cap. Therefore, the oblate spheroid surface area was applied to derive a new shape factor. Additionally, it was found that, the definition of the collisional kinetic energy in the model of Estrade et al. (1999) was not general and led to errors, for example it doubles the kinetic energy in the case of head on collisions. The definition of Hu et al. (2017) is universally applicable and conserves momentum

Using the proposed oblate spheroid shape factor, the kinetic energy definition of Hu et al. (2017) but accounting only for the mass of the interaction regions, a modified model for the bouncing regime boundary was proposed. The shape factor for head-on collisions was taken directly from measurements, and the reduction in shape factor with increasing  $B$  fitted empirically using a power law model. Viscous dissipation was also taken into account in the proposed model and for each HPMC concentration, a viscous dissipation factor was estimated directly from the experimental observations by analyzing the decay in the oscillations of bubble shape which occurs after each collision.

The proposed model shows a great fit to the experimental results. For all three HPMC concentrations the critical  $We$  number for head on collisions is well predicted and the fit to the boundary of the bouncing regime is excellent for across the range of  $We$  numbers tested, whether above or below the triple point. Quantitatively, the MAE was reduced an order of magnitude compare to the literature models.

The proposed model is considered as an important advancement in predicting the collisions' outcomes, which is very important for many applications such as spray drying. To make a better use from the model, more investigation is required to quantify the maximum deformation limit and to avoid the need for the direct measurements of the shape factor. This might need a deep understanding of the role of the intervening gas layer.

## VII. Supplemental material

Data on the droplet sphericity prior to the collisions, and about the droplet size variation due to the change of the frequency is provided.

## ACKNOWLEDGMENTS

The authors gratefully acknowledge the useful discussions and assistance of Prof Phil Threlfall-Holmes, Prof Nik Kapur and Gurdev Bhogal from the University of Leeds. The work was supported by EPSRC project: 'Evaporative Drying of Droplets and the Formation of Micro-structured and Functional Particles and Films' (grant ref: EP/N025245/1) and the University of Leeds.

## APPENDIX A: DROPLETS TRACKING METHODOLOGY

The tracking starts by uploading the high frame rate video into DMV. In DMV, the frames are cut for the region before collision point, as shown in FIG. 16. From each frame, DMV evaluates time ( $t$ ), diameter ( $d$ ), and position ( $x, y$ ) for each droplet. Every droplet is given ID number to enable the tracking of each droplet through different frames. From every two successive frames, DMV evaluates the velocity in x and y direction for each droplet, details on DMV can be found in Basu (2013). These data are saved in excel sheet, which is then loaded into MATLAB to extend the position of the droplets to the collision point. The extension procedure is as follow:

1. The ( $x, y$ ) position of the tracked droplets in frame 4 in FIG. 16 is extended with very small increment of time ( $\Delta t$ ) to become ( $x + \vec{u}_x \Delta t, y + \vec{u}_y \Delta t$ ). The increment of the time that selected in this study is  $\Delta t = d_a / 500 u_a$ .
2. The time will be updated by adding  $\Delta t$  to the time of the last frame that the tracked droplet appeared in, frame 4 in the example in FIG. 16.
3. When the newly calculated ( $x, y$ ) positions of droplets  $a$  and  $b$  satisfy  $\sqrt{(x_b - x_a)^2 + (y_a - y_b)^2} - ((d_a + d_b)/2) < 0.0001 d_a$  at  $t = t_a = t_b$ , the impact parameter will be estimated using  $B = \sin \theta$ .

The angle  $\theta$  is a function of  $(x, y)$  positions of droplets  $a$  and  $b$  and can be estimated using the following procedure considering that the frame of reference on the center of the droplet  $b$  in FIG. 16:

1. Estimating the angle between the two streams of droplets ( $a$  and  $b$ ) by using  $\theta_1 = \tan^{-1}(\vec{u}_{xa}/\vec{u}_{ya}) + \tan^{-1}(\vec{u}_{xb}/\vec{u}_{yb})$ .
2. Estimating the angle between the x axis and the line that cross the centers of the colliding droplets  $a$  and  $b$  at the collision point using  $\theta_2 = \tan^{-1}((y_a - y_b)/(x_a - x_b))$ .
3. Estimating the relative velocity using  $u_r = \sqrt{u_a^2 + u_b^2 - (2u_a u_b \cos \theta_1)}$ .
4. Estimating the angle between the relative velocity vector and stream  $b$  using  $\theta_3 = \sin^{-1}(\|\vec{u}_{xa}/\vec{u}_r\| \sin \theta_1)$
5. The angle  $\theta$  is estimated using  $\theta = 90 - \tan^{-1}(\vec{u}_{xa}/\vec{u}_{ya}) + -\theta_3 - \theta_2$ .

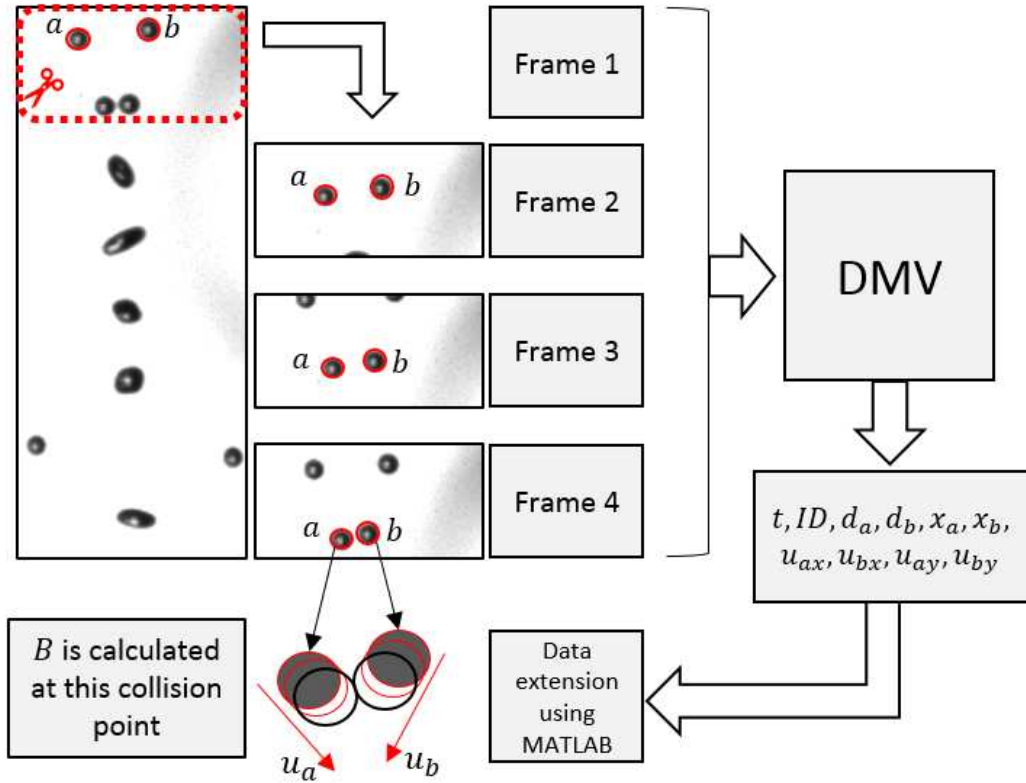


FIG. 16. Tracking methodology to estimate the collision point and hence the impact parameter.

## APPENDIX B: SPHERICAL CUP SHAPE FACTOR DERIVATION

The volume of a spherical cup is

$$V_{cup} = \frac{\pi h^2}{3} (3r_d - h), \quad (B1)$$

Where,  $r_d$  is the radius of the deformed droplet (spherical cup), and  $h$  is defined in FIG. 16. From the mass conservation, Eq. (B1) will be equal to sphere volume, hence

$$r_d = \frac{d^3}{6h^2} + \frac{h}{3}, \quad (\text{B2})$$

where,  $d$  is the diameter of the non-deformed droplet. The surface area of the spherical cup is given by

$$S. A_{cup} = \pi(4r_d h + h^2). \quad (\text{B3})$$

Substituting Eq. (B2) in Eq. (B3) and evaluating for the surface energy of colliding droplets at maximum deformation give

$$E_{sf} = \pi\sigma \left( \frac{2d_{lo}^3}{3h_l} + \frac{1}{3}h_l^2 \right) + \pi\sigma \left( \frac{2d_{so}^3}{3h_s} + \frac{1}{3}h_s^2 \right). \quad (\text{B4})$$

From mass conservation and substituting  $\phi = \frac{h}{r_d}$ ,

$$h = d_o \left( \frac{6}{\phi} - 2 \right)^{\frac{1}{3}}. \quad (\text{B5})$$

Sub (B5) in (B4) gives

$$E_{sc} = \pi\sigma d_{lo}^2 \left( \frac{2}{3} \left( \frac{6}{\phi} - 2 \right)^{-\frac{1}{3}} + \frac{1}{3} \left( \frac{6}{\phi} - 2 \right)^{\frac{2}{3}} \right) (1 + \Delta^2). \quad (\text{B6})$$

From the analogy between Eq. (B6) and Eq. (10), the correct shape factor of spherical cup is

$$\phi'_c = \frac{2}{3} \left( \frac{6}{\phi} - 2 \right)^{-\frac{1}{3}} + \frac{1}{3} \left( \frac{6}{\phi} - 2 \right)^{\frac{2}{3}}. \quad (\text{B7})$$

## REFERENCES

- Ashgriz, N. and Poo, J. 1990. Coalescence and separation in binary collisions of liquid drops. *Journal of Fluid Mechanics*. **221**, pp.183-204.
- Basu, A.S. 2013. Droplet morphometry and velocimetry (DMV): a video processing software for time-resolved, label-free tracking of droplet parameters. *Lab on a Chip*. **13**(10), pp.1892-1901.
- Estrade, J.-P., Carentz, H., Lavergne, G. and Biscos, Y. 1999. Experimental investigation of dynamic binary collision of ethanol droplets—a model for droplet coalescence and bouncing. *International Journal of Heat and Fluid Flow*. **20**(5), pp.486-491.
- Finotello, G., Kooiman, R.F., Padding, J.T., Buist, K.A., Jongsma, A., Innings, F. and Kuipers, J. 2018. The dynamics of milk droplet–droplet collisions. *Experiments in Fluids*. **59**(1), p17.
- Finotello, G., Padding, J.T., Deen, N.G., Jongsma, A., Innings, F. and Kuipers, J. 2017. Effect of viscosity on droplet-droplet collisional interaction. *Physics of Fluids*. **29**(6), p067102.
- Francia, V., Martín, L., Bayly, A.E. and Simmons, M.J. 2017. Agglomeration during spray drying: Airborne clusters or breakage at the walls? *Chemical Engineering Science*. **162**, pp.284-299.

- Gotaas, C., Havelka, P., Jakobsen, H.A. and Svendsen, H.F. 2007a. Evaluation of the impact parameter in droplet-droplet collision experiments by the aliasing method. *Physics of fluids*. **19**(10), p102105.
- Gotaas, C., Havelka, P., Jakobsen, H.A., Svendsen, H.F., Hase, M., Roth, N. and Weigand, B. 2007b. Effect of viscosity on droplet-droplet collision outcome: Experimental study and numerical comparison. *Physics of fluids*. **19**(10), p102106.
- Hu, C., Xia, S., Li, C. and Wu, G. 2017. Three-dimensional numerical investigation and modeling of binary alumina droplet collisions. *International Journal of Heat and Mass Transfer*. **113**, pp.569-588.
- Jiang, Y., Umemura, A. and Law, C. 1992. An experimental investigation on the collision behaviour of hydrocarbon droplets. *Journal of Fluid Mechanics*. **234**, pp.171-190.
- Kokubo, H. and Obara, S. 2008. Application of HPMC and HPMCAS to aqueous film coating of pharmaceutical dosage forms. *Aqueous Polymeric Coatings for Pharmaceutical Dosage Forms, Third Edition*. CRC Press, pp.299-342.
- Krishnan, K. and Loth, E. 2015. Effects of gas and droplet characteristics on drop-drop collision outcome regimes. *International Journal of Multiphase Flow*. **77**, pp.171-186.
- Kuschel, M. and Sommerfeld, M. 2013. Investigation of droplet collisions for solutions with different solids content. *Experiments in fluids*. **54**(2), p1440.
- Orme, M. 1997. Experiments on droplet collisions, bounce, coalescence and disruption. *Progress in Energy and Combustion Science*. **23**(1), pp.65-79.
- Pan, K.-L., Law, C.K. and Zhou, B. 2008. Experimental and mechanistic description of merging and bouncing in head-on binary droplet collision. *Journal of Applied Physics*. **103**(6), p064901.
- Parker, M., York, P. and Rowe, R. 1991. Binder-substrate interactions in wet granulation. 2: The effect of binder molecular weight. *International journal of pharmaceuticals*. **72**(3), pp.243-249.
- Qian, J. and Law, C. 1997. Regimes of coalescence and separation in droplet collision. *Journal of Fluid Mechanics*. **331**, pp.59-80.
- Sommerfeld, M. and Kuschel, M. 2016. Modelling droplet collision outcomes for different substances and viscosities. *Experiments in Fluids*. **57**(12), p187.
- Sommerfeld, M. and Lain, S. 2017. *Numerical analysis of sprays with an advanced collision model*.
- Tang, C., Zhang, P. and Law, C.K. 2012. Bouncing, coalescence, and separation in head-on collision of unequal-size droplets. *Physics of Fluids*. **24**(2), p022101.
- Xia, S.-y. and Hu, C.-b. 2014. Numerical investigation of head-on binary collision of alumina droplets. *Journal of Propulsion and Power*. **31**(1), pp.416-428.
- Zhang, P. and Law, C.K. 2011. An analysis of head-on droplet collision with large deformation in gaseous medium. *Physics of Fluids*. **23**(4), p042102.